Unraveling the Nanoscopic Strain Evolution in Single Crystal Cathodes

Jing Wang[1,2], Tongchao Liu[1], Weiyuan Huang[1], Lei Yu[3], Tianyi Li[4], Xiaojing Huang[5], Xianghui Xiao[5], Lu Ma[5], Tao Zhou[3], Martin V. Holt[3], Haozhe Zhang[1,2], Rachid Amine[6], Wenqian Xu[4], Luxi Li[4], Jianguo Wen[3], Ying Shirley Meng[2,7*], Khalil Amine[1,2*]*

[1]*Chemical Sciences and Engineering Division, Argonne National Laboratory, Lemont, IL 60439, USA*

[2]*Pritzker School of Molecular Engineering, University of Chicago, Chicago, Illinois, 60637, USA*

[3]*Center for Nanoscale Materials, Argonne National Laboratory, Lemont, IL 60439, USA*

[4]*X-ray Science Division, Advanced Photon Sources, Argonne National Laboratory, Lemont, IL 60439, USA*

[5]*National Synchrotron Light Source II, Brookhaven National Laboratory, Upton, NY 11973, USA*

[6]*Material Science Division, Argonne National Laboratory, Lemont, IL 60439, USA*

[7]*Argonne Collaborative Center for Energy Storage Science (ACCESS), Argonne National Laboratory, Lemont, IL 60439, USA.*

**Corresponding author. Email: liut@anl.gov (T. L.); shirleymeng@uchicago.edu (Y. S. M.); amine@anl.gov (K. A.).*

Abstract

Single-crystal layered oxides (SC-NMC) with grain boundary-free configuration, have effectively addressed the long-standing cracking issue of conventional polycrystalline Ni-rich cathodes (PC-NMC) for lithium-ion batteries, prompting a shift in optimization strategies. However, continued reliance on anisotropic lattice volume change—a well-established failure indicator in PC-NMC—as a metric for understanding lattice strain and guiding compositional designs for SC-NMC becomes contentious. Herein, leveraging multi-scale diagnostic techniques, we unraveled the distinct nanoscopic strain evolution in SC-NMC cathodes, challenging the conventional composition-driven strategies and mechanical degradation indicators used for PC-NMC. Through particle-level chemo-mechanical analysis , we reveal a decoupling between mechanical strain and lattice volume change of SC-NMC, identifying that the structural instability in SC-NMC is primarily driven by multiple-dimension lattice distortions induced by kinetics-driven reaction heterogeneity and progressively deactivating chemical phases. Consequently, the roles of cobalt (Co) and manganese (Mn) in SC-NMC have been redefined based on the newly established mechanical failure mode. Unlike cobalt's detrimental role in PC-NMC, we find Co to be critical in enhancing the longevity of SC-NMC cathodes by mitigating localized

lattice strain along extended diffusion pathway, whereas Mn exacerbates mechanical degradation. Our findings fundamentally redefine the compositional requirements for SC cathodes compared to conventional NMC cathode systems, offering new insights into developing mechanically robust electrode materials with high capacity and superior durability.

Main text

Nickel-rich $LiNi_xMn_yCo_zO_2$ ($x+y+z=1, x\geq 0.6$, Ni-rich NMC) cathode materials with high accessible capacity (>200 mAh g^{-1}) have been widely used in high-energy lithium-ion batteries (LIBs)[1-4]. However, mechanical degradation in Ni-rich cathodes, primarily driven by external stress or internal lattice strain, poses a critical challenge for their advancement[5-8]. This degradation often leads to particle fracture, followed by surface parasitic reactions and irreversible phase transformation[9,10]. Especially, most of the existing commercial Ni-rich cathodes are secondary particles composed of primary nanograins connected by grain boundaries[11,12]. Such PC-NMC cathodes are inherently susceptible to mechanical instability because of the anisotropic lattice parameter changes (i.e., expansion along c direction and contraction along a/b direction) during Li moving in and out of lattice[13]. The repeated volume expansion and contraction during battery cycling subject the randomly oriented nanograins to severe compressive or tensile strain through the interactions between closely packed particles. The strain can be further exacerbated by the large lattice parameter changes and crystallographic anisotropy within the nanograins[14,15]. This inevitably creates intergranular cracks, facilitating electrolyte penetration to the newly exposed surface and triggering additional interfacial degradation[16-18]. Accordingly, the magnitude of volume change becomes a common indicator for accessing strain accumulation and mechanical stability of PC-NMC cathodes[8,14,19-24].

To mitigate the mechanical degradation issue, modulating lattice volume evolution by optimizing cobalt (Co) and manganese (Mn) content in PC-NMC cathodes has been widely explored as the changes of composition could substantially alter electrochemical properties. Typically, Co mitigates Li/Ni disorder but promotes particle cracking due to exacerbated volume change and high lattice oxygen activity at deep delithiation states[5,19,25,26]. Conversely, Mn constrains lattice parameter changes and improves interfacial stability with stable Mn(IV)-O bonds in NMC lattice, which comes at the cost of lower initial capacity[19,27,28]. Consequently, low Co and even Co-free NMCs are considered a feasible roadmap to enhance structural stability of Ni-rich cathodes at less cost[29-31]. While the grain

boundaries still exist, it poses potential risks for particle pulverization and surface deterioration especially at high voltage operations.

Single crystallization has emerged as a promising strategy to enhance multiscale structural integrity of NMC particles through the removal of grain boundaries.[32,33] The SC architecture not only facilitates higher tap density at electrode level but also alleviates differential stresses within the crystal lattice and reduces surface reconstruction at cathode-electrolyte interface. However, the larger crystal size (2-10 μm) inherent to SC particles significantly magnifies the impact of nanoscopic lattice strain, primarily driven by heterogeneous Li^+ (de)insertion through the extended diffusion pathways within the layered structure.[34,35,36] Despite this, current understanding and characterization of lattice strain in SC-NMC are often based on models developed for PC-NMC, where volume change serves as a key indicator of mechanical strain.[37-40] Nonetheless, the actual volume change-strain-performance (VSP) relationship in single particles, free from the grain-to-grain compressive/tensile stresses characteristic of PC cathodes, is largely underexplored. Consequently, the composition-driven strain engineering strategies for SC Ni-rich cathodes may not align with previous observations in PC systems. Yet, there has been limited investigation into the actual strain evolutions in SC particles. This gap is further compounded by the absence of methodically integrated, multiscale diagnostics techniques, which are essential for capturing how strain develops, evolves, and impacts the structural stability and electrochemical performance.

Herein, we systematically investigate the interplay between lattice volume changes, nanoscopic strain, and electrochemical failure in SC Ni-rich cathodes, using both PC and SC Co-free $LiNi_{0.9}Mn_{0.1}O_2$ (NM91) and Mn-free $LiNi_{0.9}Co_{0.1}O_2$ (NC91) as model systems. Through multi-scale characterizations, we elucidate the distinct strain evolution in SC Ni-rich cathodes, challenging previously established VSP relationship for conventional NMC cathodes. We reveal that large volume change is not the prerequisite for severe lattice strain (or lattice distortion); rather, the root cause lies in kinetically driven reaction heterogeneity. The presence of lattice strain further exacerbates localized chemical and mechanical degradation, leading to capacity decay over cycling. Notably, contrary to previous observations in PC cathodes, we demonstrate that Mn is more mechanically detrimental than Co in SC Ni-rich cathodes. This is attributed to more heterogeneous intra-particle reaction and more severe lattice strain accumulation stemming from sluggish kinetics in Co-free cathodes. Conversely, Co proves essential in SC cathodes for improving capacity and structural stability, striking a promising balance between cost, performance, and

sustainability. By simultaneously probing chemical and mechanical aspects at both nano- and micron- scale, our work has provided novel insights into compositional optimization pathways in SC cathodes, guiding the rational development of high-performance cathode materials with long-cycle life.

Strain evolution in PC Ni-rich cathodes

The strain in PC Ni-rich layered oxides is predominantly induced by anisotropic volume changes during cycling. The magnitude of expansion or contraction along a-lattice direction is directly correlated with the ionic radius of redox species (i.e., Ni ions for Ni-rich layered oxides), while the c-lattice spacing change is critically governed by the electrostatic interaction at adjacent oxygen layers (i.e., O–O and O–Li–O). Given relatively small and consistent change of a-lattice parameters during Ni oxidation/reduction, the strain in PC NMC cathodes can be modulated by tuning Mn/Co ratio. To investigate the VSP relationships for strategic composition-driven strain regulation in insertion chemistry, we have designed two comparable compositions, Co-free NM91 and Mn-free NC91 as our models, featuring boundary-rich or boundary-free configurations. The same Ni content ensures a comparable state of charge (SoC), while the variations of Mn/Co content allow for controlled regulation of lattice dimension changes. The VSP relationships are examined for conventional PC cathodes at inter-particle level and further explored for SC Ni-rich layered oxides at intra-particle level.

The Ni-rich cathode materials were prepared by a conventional co-precipitation and solid-state calcination process. SEM images (Supplementary Fig. 1) show that both PC-NC91 and PC-NM91 cathodes have uniform secondary-particle morphologies with a similar particle size of 10 μm. The SC cathodes, characterized by boundary-free crystal structures, exhibit particle sizes ranging from 3 to 5 μm (Supplementary Fig. 2). The four cathodes share a typical hexagonal α-$NaFeO_2$ layered structure with $R\bar{3}m$ symmetry, without any detectable impurity phases (Supplementary Fig. 3, Supplementary Table 1-4). A higher degree of Li/Ni disorder is found in Co-free cathodes compared to Mn-free cathodes, which is typically be attributed to a slightly stronger magnetic frustration present in Ni^{2+}/Ni^{3+} and Mn^{4+}.[41]

To understand the VSP relationships in PC layered oxides, lattice parameter evolutions are observed by in situ XRD measurements, which allows for a qualitative comparison of mechanical stiffness across PC-NC91 and PC-NM91 during charge and discharge. Fig. 1a-b show the two-dimensional (2D) contour plots of PC-NC91 and PC-NM91 cathodes during the first cycle at 0.1C. Both samples show a similar SoC dependent shift during

delithiation and lithiation, indicating the solid-solution reactions in the layered structure. Specifically, as shown in Supplementary Fig. 4 and 5, the (003) peaks of both cathodes shift to lower angles before 4.1 V, indicating a gradual expansion of the c-axis induced by the columbic repulsion between the adjacent oxygen layers within the delithiated unit cell[42-43]. Afterwards, the (003) peaks markedly shift right until the end of charge to 4.5V, which is related to the phase transition from H2 to H3 phase with a rapidly reduced interlayer spacing[44-45]. Rietveld refinements were applied to quantitatively compare the anisotropy of dimension change and magnitude of compression/tensile stress between the two PC cathodes. To describe anisotropy of lattice change, the normalized unit cell parameter c/c_0 during cell charge is plotted against ab/a_0b_0 ($a = b$ for layered structure) in Fig. 1c. The isotropic change of lattice is indicated by the gray line which shows a linear variation of c-lattice spacing with the dimensional change at a-axis direction. PC-NC91 exhibits a larger deviation from the isotropic change compared to PC-NM91, indicating a faster build-up of mechanical stress between primary grains during charging through distortion of crystal lattice. The similar dimension changes along the a-axis indicate the comparable oxidation state changes of Ni ions during charging (Supplementary Fig. 6). Notably, more marked lattice parameter change along c-axis (6.0%) is observed in PC-NC91 compared to PC-NM91 (3.6%), accompanied by a more pronounced overall volume shrinkage in Co-containing cathode (7.8% vs 5.9%), as shown in Fig. 1d and Supplementary Fig. 7. The larger magnitude of volume change suggests a more severe compression/tensile stress at grain boundaries due to the different crystallographic orientations of primary particles.

Ex situ postmortem focused ion beam-scanning electronic microscopy (FIB-SEM) is carried out to correlate the mechanical strain with morphological evolution in both PC cathodes. The PC-NC91 exhibits apparent microcracks along the grain boundaries, expanding throughout the entire secondary particles (Fig. 1e). The cracks inside the PC-NC91 facilitate the electrolyte infiltration and parasitic reactions within the particle interior. The PC-NM91, on the other hand, remains largely intact, exhibiting only minor vein-like features after 100 cycles, indicating superior morphological stability (Fig. 1f). Consequently, PC-NM91 shows an improved cycling stability (83.1%), attributing to the reduced grain separation and intergranular cracks (Fig. 1g). Conversely, PC-NC91 suffers from rapid performance degradation with a capacity retention of 59.7% after 100 cycles. Anisotropic lattice distortion and volume contraction, which are directly linked to mechanical strain within PC particles, promote particle fracture and grain boundary

separation, ultimately leading to the deterioration of layered oxides. This process defines the typical VSP relationships in PC Ni-rich cathodes (Fig. 1h).

Clearly, the established VSP relationships in PC cathodes are predominantly based on the grain-to-grain interactions—including mechanical stress accumulation and boundary separation— that arise from anisotropic volume changes in the secondary particles. However, in SC Ni-rich cathodes, where grain boundaries are absent (Fig. 1i), the role of volume change on structural evolution remains less understood. This uncertainty influences the strategies for strain management and composition design within a SC framework. As shown in Fig. 1j, the long-term cycling performance of the SC-NM91 and SC-NC91 cathodes was evaluated under the same testing conditions as their PC counterparts. Interestingly, SC-NC91 demonstrates superior cycling stability with a capacity retention of 89.2% after 100 cycles, compared to the significantly lower retention of 75.9% for SC-NM91. These results contrast with prior studies of PC Ni-rich materials, where the cycling stability of Co-free cathodes outperformed the Mn-free, Co-substituted ones, necessitating further exploration into the strain dynamics in SC materials.

Self-accelerated phase transition in SC Ni-rich layered oxides

To track the lattice structure evolution in SC cathodes, synchrotron-based operando XRD measurements were performed on SC-NM91 and SC-NC91 during the first cycle, using the same testing procedures. The voltage profiles and corresponding dQ/dV curves for phase transitions are shown in Supplementary Fig. 8. As indicated in Fig. 2a and Supplementary Fig. 9, same with the PC Ni-rich cathodes, SC-NC91 shows a SOC dependent shift during charging, exhibiting the solid-solution reactions. At the high-delithiated states, SC-NC91 maintains the single-phase H2-H3 transition with minimal changes in intensity and width of (003) peak, suggesting a uniform lattice structure at high voltage. By contrast, substantial peak broadening of (003) peak is shown in SC-NM91 which starts from 4.1 V and persists at the end of charging, suggesting the presence of multiple phases (Fig. 2b and Supplementary Fig. 10). Notably, the phase segregation of SC-NM91 mainly occurs at highly delithiated states, which may be attributed to the unsynchronized H2 to H3 phase transition inside particles due to the sluggish kinetics.

Galvanostatic intermittent titration technique (GITT) and four-point probe conductivity measurements were conducted to investigate the impact from electronic conductivity and ion diffusion during charging. As indicated in Supplementary Fig. 11, significant disparity is observed in electronic conductivities between SC-NM91 (0.75 mS cm^{-1}) and SC-NC91

(2.85 mS cm^{-1}) pristine powders. Moreover, SC-NM91 experiences a rapid drop in Li^+ diffusion rate during delithiation starting from 50% SoC (4.0V), with the D_{Li+} more than four times lower than that of SC-NC91 at the end of charging (Supplementary Fig. 12). As shown in Supplementary Fig. 13**,** SC-NC91 exhibits superior rate capability compared to SC-NM91, with higher capacity and better cycling stability at different current densities (0.1C, 0.2C, 0.33C, 0.5C, 1C and 2C). This observation indicates the intrinsic difference in Li diffusion and reaction rate influenced by Mn/Co content, which aligns well with previous reports regarding Ni-rich cathodes[27]. The impact from these intrinsic kinetic variations could be further amplified by the long diffusion pathways in the SC cathodes.

To understand the kinetic effects in phase evolution, in-situ XRD of both cathodes were measured at a higher current density at 1 C (Fig. 2c-d). In SC-NC91, the accelerated charge/discharge rate obscures the H2-H3 phase transition due to the reduced delithiation (Fig. 2c, Supplementary Fig. 14). Yet, the (003) reflections maintain a single-phase evolution with a nearly symmetrical shape until the end of charging, suggesting homogeneous lattice structure across the particles in SC-NC91, even under rapid Li extraction/insertion. Interestingly, in SC-NC91, the peak positions at 1C align with that achieved at the same SoC when charging under 0.1C (corresponding to 78% SoC; define 270 mAh g^{-1} for a nominal 100% SoC), indicating a good correlation between the peak position and delithiation states (Fig. 2h, left). However, for SC-NM91, more pronounced peak broadening and separation emerge from 4.3 V, presenting H2-H3 phase transition process (Fig. 2d, Supplementary Fig. 15). Though with only 78% of capacity (66% SoC) at 0.1C, the maximum c-lattice parameter change exhibited at 4.5V of 1 C closely matches the maximum value observed at 0.1 C (85% SoC), indicating partially deep delithiated phases can be reached inside particles. The fast reaction rate exacerbates lattice parameter changes and phase separation in SC-NM91, as indicated by a more right-shifted peak at 1C compared to that delithiated at 0.1C with same SoC (Fig. 2h. right). Consequently, the difference of capacity retentions of SC-NC91 and SC-NM91 cycled at 1C (15%) becomes larger than that at 0.5C (13.3%), as shown in Supplementary Fig. 16.

Rietveld refinements were applied to the in situ XRD data to distinguish and index the phases in both SC-NC91 and SC-NM91 at high delithiated states. The (003) reflections were deconvoluted by assuming a single-phase or coexistence of multiple phases, as demonstrated in Fig. 2a-d, and the quantitative refinement results on a- and c-lattice parameters are shown in Fig. 2e-g. The two materials show a similar change of a-lattice, indicating a comparable degree of Ni oxidation during charging. Notably, SC-NC91

exhibits a similar lattice parameter change with PC-NC91 of around 5.9% and maintained single phase evolution. However, SC-NM91 presents an obvious two-phase coexistence (denoted as sluggish phase and accelerated phase, respectively) region at a high degree of delithiation. The accelerated phase shows a larger c-spacing change (4.2%) compared to PC-NM91, while the sluggish phase exhibits a much smaller change (1.8%). The sluggish Li ion diffusion in SC-NM91 with long diffusion length leads to the co-existence of H2-H3 phase, distinguished by significant differences in lattice parameters (Δc_{max} = 0.68 Å) in bifurcated peaks. Observations of the operando phase transitions at different current densities suggest a self-accelerating reaction within the SC particle. The outer 'shell' reaches the H3 phase earlier, with a more contracted lattice, blocking Li-ion movement from the core. Driven by the constant current charging, the already-reacted regions undergo further delithiation, forming more contracted layers, which exacerbates ion transport limitations in the sluggish phases. This self-accelerating process is induced by continuous Li extraction from the non-equilibrium lattice structure, which is further aggravated by higher cut-off voltages and elevated reaction rates (Fig. 2h).

Different from PC Ni-rich cathodes, a larger lattice parameter change but more homogeneous phase evolution in SC-NC91 during Li extraction/insertion results in better cycling stability than SC-NM91 with smaller lattice change. Thus, the electrochemical stability in SC cathodes is predominantly independent of lattice dimension change, but rather closely linked to the intra-particle crystallographic homogeneity. Further investigations using spatial resolution techniques are essential to correlate phase separation, lattice parameter changes observed in electrode-level XRD, with the lattice strain as well as chemical structure occurring at the particle level.

Nanoscale mapping for localized lattice and chemical structure

Nano-focused Scanning X-ray Diffraction Microscopy (SXDM) with high spatial and structure resolutions was performed to analyze lattice strain within single particles of SC-NM91 and SC-NC91. As illustrated in Fig. 3a, the particles were illuminated with the nanofocused X ray beam (~30 nm spot size) and rocked in the vicinity of the selected Bragg reflection (two-degree range). At each rocking angle, a 2D raster scan was performed, collecting 3D diffraction patterns from each scan position recorded in the oriented pixel-array detector[46]. By fitting the Bragg diffraction peak position at each scanned point, lattice distortions can be analyzed from the extracted crystallographic structural parameters. Fig. 3b illustrates three types of observed lattice distortions from SXDM: lattice strain

(interlayered expansion/contraction), lattice twisting in Y direction and bending in Z direction. The lattice variation evaluated by Δd/d can be attributed to different d-spacing values in the layered phases, while crystallographic rotation/tilt arises from the lattice misorientations. Detailed description of the SXDM method is presented in the method section.

The results of SXDM mapping for the two samples charged to 4.5V are shown in Fig. 3c-d, which presents d-spacing variation, lattice twisting and bending in y and z direction, respectively. The charged SC-NC91 particle exhibits a homogenous lattice structure characterized by a narrow d-spacing distribution with a maximum variance of 0.003. The total diffraction intensity mapping for the charged SC-NC91 indicates high crystalline quality with a uniform and strong intensity over the whole particle (Supplementary Fig. 17). This is consistent with the observation at in-situ XRD data where it shows single-phase solid solution behavior during charging, indicating synchronous phase evolution and small lattice strain introduced during the delithiation process. By contrast, the total diffraction intensity for the charged SC-NM91 is less detectable except for the center, suggesting a significantly decreased crystalline quality (Supplementary Fig. 18). The SXDM mapping confirms that the charged SC-NM91 particle shows obviously severe lattice distortion, with a large interlayer spacing variation of 0.008—four times larger than that of SC-NC91, which shows a variation of only 0.002. This is well aligned with the evident (003) peak separation in the XRD data at high SoCs, suggesting the coexistence of two phases with distinct lattice parameters (phase H2 and H3) exacerbating lattice strain inside particles. Additionally, higher magnitudes of twisting and bending are observed in SC-NM91 compared to SC-NC91, which points to larger crystal orientations or rotations generated during charging.

It Is noticed that for both SC cathodes, the lattice strain is increased while the lattice rotation (twisting and bending) is decreased after long-term cycling (Fig. 3g-i). This may be attributed to the gradual release of misorientation distortion caused by the irreversible phase transitions to spinel and rock-salt phases. However, lattice strain can intensify due to the increased lattice mismatch between the newly formed rock-salt/spinel phases and the remaining layered structures, which can further exacerbate structure heterogeneity. The magnitude of interlayer spacing heterogeneity and lattice misorientation of SC-NC91 is still at relatively low level after cycling, suggesting the superior structural stability (Fig. 3e). The lattice distortions are mainly located near particle surface, which may arise from commonly observed lattice mismatch at cathode-electrolyte interface[16]. However, lattice

strain in SC-NM91 becomes significantly more pronounced after cycling, with d-spacing heterogeneity 3.3 times larger than that of SC-NC91, accompanied by a marked reduction in twisting and bending distortions. This suggests a lattice strain-dominated degradation over long-term cycling (Fig. 3f). Interestingly, while SC-NC91 shows more significant change in c lattice parameter than that of SC-NM91 at fully delithiated states as indicated by in-situ XRD, it exhibits less severe lattice distortion and more stable lattice structure. This observation implies that lattice strain is not directly tied to the magnitude of lattice parameter changes but could be closely attributed to deviations of local crystal lattice from the expected states at different SoCs. Similarly, the structure degradation is not showing a dependance on the magnitude of lattice expansion/contraction but is more related to the gradual accumulation of lattice strain inside SC particles.

Based on the above observations, lattice strain is decoupled from lattice parameter change of single crystals. However, further investigation is required to fully understand how lattice strain contributes to the mechanical degradation of particles. To build a relationship between phase evolution behavior with chemical properties of both samples, X-ray absorption spectroscopy (XAS) was employed for the first charge/discharge cycle. As shown in Supplementary Fig. 19, there are minimal changes at the Mn and Co K-edges, suggesting that Mn and Co ions remain electrochemically inactive, not contributing additional capacity. Meanwhile, both SC-NM91 and SC-NC91 demonstrate a relatively reversible Ni oxidation/reduction during the initial charge/discharge cycle, with the Ni K-edge shifting back to the pristine state, as indicated in Supplementary Fig. 20. Thus, the chemical evolution detected by the electrode-level characterization technique is not adequate to explain the significantly different electrochemical performance between them after long-term cycling. An in-depth investigation into the chemical structures for the two cathodes at the particle level is required.

Full-field transmission X-ray microscopy (TXM) coupled with 3D X-ray absorption near-edge spectra (XANES) was further conducted to analyze the chemical origins that give rise to lattice strain in SC Ni-rich cathodes. Fig. 4a-b show the Ni oxidation state distribution (manifested by color variations with a 40 nm resolution) for charged SC-NC91 and SC-NM91 at 4.5 V, based on the white-line (WL) energy shift of Ni K-edge. The cross-section chemical mappings from three different directions (i.e., xy, yz and xz) demonstrate a homogeneous Ni valence across the SC-NC91 particles (Fig. 4a). By contrast, a large portion of the charged SC-NM91 particles exhibit high oxidation states within the bulk (Fig. 4b). The histogram for statistical analysis of each 3D dataset is shown in Fig. 4c-d for

SC-NM91 and SC-NC91. The mean peak position indicates the average SoC within the particles, lower white-line energy suggests a less oxidized Ni state, while the peak shape/width describes the heterogeneity of SoC distribution. SC-NC91 shows a higher average WL energy than SC-NM91, which is consistent with the XAS data obtained at the electrode level (Supplementary Fig. 21). However, a sharper peak is observed for SC-NC91, suggesting the homogeneous SoC distribution inside particles. SC-NM91 has a wide Ni oxidation state distribution, indicating a more heterogeneous delithiation reaction within the particle. With the average SoC of 85% at 4.5V, parts of the SC-NM91 particle reach deeper delithiated states (> 91% SoC) than SC-NC91 indicated by the presence of a higher Ni oxidation valence, while some parts are still in low SoCs. Notably, the higher SoC is typically linked to exacerbated lattice shrinkage. The wider SoC distribution implies the coexistence of chemical phases with huge disparity of lattice constants, inducing severe lattice strain inside particles[36]. Moreover, the deep delithiated states triggered by inhomogeneous reaction inside particles may contribute to irreversible lattice distortions arising from σ-type hybridization between Ni^{3+}/Ni^{4+} and the O^{2-} species[47]. The broad distribution of Ni valence states is in good corresponding with the peak separation in SC-NM91 observed in the in-situ XRD, as well as the large d-spacing heterogeneity in SXDM strain mapping.

Fig. 4e-f show the 3D TXM-XANES results of both samples after cycling. Even though more lithium is extracted from SC-NC91 at each cycle, it still exhibits uniform Ni oxidation state in particles, indicating the good reaction reversibility and well-maintained chemical structure. Nonetheless, more red regions are observed for SC-NM91 even it is in discharged state, suggesting the existence of inactive Ni-related phase and thus explaining the capacity loss of SC-NM91 over cycling. The formation of electrochemically fatigued phases in SC-NM91 may be linked to the release of misorientation distortion and escalation of localized lattice strain, as demonstrated in SXDM analysis. The overall Ni valence in the cycled SC-NM91 particles appears increased due to the irreversible Li extraction and insertion, as evidenced by XAS data (Fig. 4g, Supplementary Fig. 22). Further statistical analysis of the WL peak position shows wider Ni valence distribution of SC-NM91 than SC-NC91 (Fig. 4h). Thus, it is clear that the inhomogeneous Ni oxidation and delithiation during charging promotes the generation of deep delithiated phases with highly oxidized Ni species, which eventually lead to irreversible chemical structure change.

Atomic-scale observation of strain accumulation in SC Ni-rich cathodes

The investigation into the impact of lattice strain and reaction heterogeneity on morphology and lattice structure was conducted using high resolution transmission electron microscopy (HRTEM). The low-magnification observations (Fig. 5a,g) reveal that, after prolonged cycling, the surface structures of both samples underwent a transformation into a rock-salt phase. This transformation should be attributed to the surface parasitic reduction between Ni^{4+} reactions and carbonate electrolyte. It's worth noting that such surface phase transformations are commonly observed in Ni-rich layered oxides and appear to be independent of the Mn and Co content[19,48]. When move the observation to the subsurface regions, distinct structural differences emerge in the evolution of SC-NM91 and SC-NC91 during cycling. As depicted in Fig. 5b-d and Supplementary Fig. 23, SC-NC91 maintains an intact structure without any observable microcracks. Conversely, the cycled SC-NM91 exhibits notable morphological damage, and evident intragranular cracks, as well as the presence of a rock-salt phase near the cracks (Fig. 5h-j, Supplementary Fig. 24). Furthermore, Fig. 5k and 5l illustrates a significant distribution of lattice strain across the selected areas of SC-NM91, revealing substantial lattice strain primarily concentrated in the cracking region. As shown in Supplementary Fig. 25, the O K-edge pre-peak not only decreases near the surface of SC-NM91 but also exhibits a relatively low intensity across the cracks. This suggests that lattice strain plays a crucial role in mechanical degradation, leading to localized oxygen loss with additional inactive rock-salt phase formation in the bulk. In contrast, SC-NC91 exhibits a more uniform lattice structure with minimized strain accumulation and structural distortion (Fig. 5e and 5f). Despite experiencing a larger lattice parameter change during Li extraction/insertion, the bulk structure of SC-NC91 retains its characteristic layered arrangement without observing mechanical failures. This phenomenon further confirms that nanoscopic lattice strain is the primary factor contributing to the mechanical failure and performance degradation of SC Ni-rich cathodes.

Composition-driven strain engineering in SC Ni-rich cathodes

Based on the comprehensive comparisons of SC-NM91 and SC-NC91 covering from electrochemistry, chemo-mechanical properties, and microstructure evolution, it is evident that the strain evolution in SC Ni-rich cathodes substantially differ from that in PC Ni-rich cathodes, which eventually alters the roles of Co and Mn on electrochemical performance. The chemo-mechanical evolutions of the two compositions are summarized in Fig. 5m. Co is found to be beneficial for mechanical stability and cycling performance in SC Ni-rich

cathodes due to the superior kinetics, while the Co-free SC-NM91 cathodes suffer from fast capacity decay and structure degradation. This discrepancy largely associates with their distinct chemo-mechanical evolutions during delithiation/lithiation, especially at the high SoCs where the large lattice strain is observed. The generation of intragranular strain may lie in the mismatch of the reaction rate (driven by constant current) and the equilibration rate (driven by Li diffusion) inside particles, which is exacerbated at the high delithiated states and increased current density. The lattice mismatch and the current-driven reaction force the already-reacted parts in SC particles to react further and generate contracted lattice layers (self-accelerated phases). The distorted lattice, characterized by significant lattice strain and misorientation, further impedes the Li diffusion in the sluggish phases. Thus, the formation of a more pronounced non-equilibrium structure leads to lattice contraction initiating at a lower SoC at 1C rate, compared to that observed at 0.1C. Though the average of SoC of SC-NM91 (85%) is lower than SC-NC91 (91%) at charged state, parts of particle exhibit even higher SoCs (>91%) with higher Ni valence at the Co-free samples. The deeper delithiated parts with higher Ni valence species induce more severe degradation at bulk lattice by O loss and phase transformation through reduction reaction with electrolyte[49,50]. Lattice rotation is largely alleviated by phase transitions, while lattice strain progressively accumulates, ultimately leading to chemical and mechanical degradation. As a result, severe particle cracking and pulverization are generated in SC Co-free cathode even after one cycle (Supplementary Fig. 27). On the other hand, SC-NC91 enables the fast equilibrium, mitigating the inhomogeneous reaction as well as lattice distortion during delithiation. Therefore, less intragranular cracking and gliding are observed in SC-NC91 (Supplementary Fig. 28), even it has a more significant volume change during charge and discharge. Thus, unlike in PC Ni-rich cathodes, a larger volume change is not necessarily a prerequisite for more pronounced lattice strain in SC cathodes. Rather, the kinetics-driven reaction heterogeneity induces localized strain of crystal domains within particles, contributing to the formation of mechanical failure and diminished electrochemical performance. These apparent discrepancies of compositional effects between SC cathodes compared to previous view in PC ones indicate the importance of understanding strain evolution at single-particle level to effectively modulate their chemical and mechanical properties.

Discussion

Overall, by integrating multiple diagnostic techniques, we have uncovered the distinct nanoscopic strain evolution in SC Ni-rich cathodes, leading to a redefinition of composition effects. Differing from their PC cathodes, the strain in SC cathodes is decoupled from the magnitude of lattice parameter changes. Instead, the reaction heterogeneity can lead to auto-accelerated delithiation inside particles, resulting in localized regions of intensified strain generation, ultimately diminishing electrochemical performance. Furthermore, we observed that the compositional effects deviate significantly from the observations in PC cathodes. Mn exacerbates reaction inhomogeneity and lattice strain in micron-scale particles, while Co enables fast structural equilibrium and synchronous phase transition during battery charge/discharge cycles. As a result, Co-containing SC cathode shows a higher specific capacity, improved cycling stability and good rate capability, demonstrating the promising design strategies for SC cathode materials with rapid kinetics and durable architectures. These results not only elucidate the distinct strain modulation pathways compared to convention NMC, but also re-define the role of Mn and Co in SC cathodes, thereby paving the way for compositional/structural optimization towards a practical trade-off between cost, performance, and sustainability.

Method

Materials synthesis: $Ni_{0.9}Mn_{0.1}(OH)_2$ and $Ni_{0.9}Co_{0.1}(OH)_2$ precursors were prepared using a co-precipitation method in a 4 L batch reactor. Stoichiometric quantities of $NiSO_4 \cdot 6H_2O$ (Sigma-Aldrich, ≥98%) with either $MnSO_4 \cdot H_2O$ (Sigma-Aldrich, ≥99%) or $CoSO_4 \cdot 7H_2O$ (Sigma-Aldrich, ≥99%) were dissolved in deionized water to form 2 M solutions. The transition metal sulfate solutions were pumped into the reactor, along with 4 M NaOH and 6 M $NH_3 \cdot H_2O$ serving as a chelating agent. The reactions occurred under a nitrogen atmosphere, with the pH maintained at 11.5, stirring at 1000 rpm, and temperature controlled at 60°C. Afterward, the precursor powders were washed, filtered, and vacuum dried at 80°C overnight. The precursors were then thoroughly combined with $LiOH \cdot H_2O$ as the lithium source (Li: TM= 1.03:1). PC-NM91 was synthesized by sintering $Ni_{0.9}Mn_{0.1}(OH)_2$ at 740°C for 12 hours at a heating rate of 2°C min^{-1} under an O_2 atmosphere. PC-NC91 was synthesized by sintering $Ni_{0.9}Co_{0.1}(OH)_2$ at 720°C for 12 hours at the same heating rate and atmosphere. SC-NM91 was synthesized by sintering $Ni_{0.9}Mn_{0.1}(OH)_2$ at 900°C for 2 hours, followed by 870°C for 10 hours at a heating rate of

4°C min^{-1} under an O_2 atmosphere. Similarly, SC-NC91 was obtained by sintering $Ni_{0.9}Co_{0.1}(OH)_2$ at 880°C for 2 hours and 850°C for 10 hours under identical conditions. Finally, the powders were carefully ground to produce the products.

Electrochemical measurements: Electrodes used in this work were prepared by mixing the active materials with carbon black (C45 Conductive Carbon Black, TIMCAL) and polyvinylidene fluoride (PVDF, Solvay® 5130) binder dissolved in n-methyl-2-pyrrolidone (NMP) in an 80:10:10 mass ratio. The mixture was ground in a mortar at 2000 rpm for 8 minutes, and the resulting slurry was cast onto aluminum foil. To form the cathode, the slurry coated foils were dried at 75 °C for 2h and then rolling pressed. The cathodes were then dried in vacuum oven at 60 °C for overnight before testing. The mass loading of cathode materials was ~4 mg cm^{-2}. The 2032 type coin half-cells were assembled using Li metal foil as anode, Celgard 2325 as separators, and 1.2 M $LiPF_6$ in EC/EMC (3:7) as electrolyte. Galvanostatic charge-discharge cycling was performed using a NEWARE battery testing system at a constant temperature of 25 °C. Three formation cycles at 0.1C were conducted before the long-term cycling test at 0.5C. Galvanostatic intermittent titration technique (GITT) measurements were taken at 0.1C in the voltage range of 2.8–4.5 V with a Maccor electrochemical analyzer. The electronic conductivity of SC-NM91 and SC-NC91 electrodes or powders was evaluated at 25 °C using a four-point probe, stepping the voltage to 4.0 V with a target current of 100 μA.

Structural characterization: Scanning electron microscopy (SEM) was performed using a Hitachi S4700 at Center for Nanoscale Materials of Argonne National Laboratory. High-energy X-ray diffraction (HEXRD) data in the form of two-dimensional diffraction patterns were collected at the 11-ID beamline (0.1665 Å) and the 17-BM beamline (0.4520 Å) of the Advanced Photon Source at Argonne National Laboratory using a Perkin-Elmer large-area detector. Rietveld refinements were processed using the GSAS-II software package. X-ray absorption spectroscopy (XAS) experiments were conducted at the 7-BM-B beamline of the National Synchrotron Light Source II (NSLS-II) at Brookhaven National Laboratory. All the XAS spectra were collected under room temperature with the transmission signals. Cross-sectional samples were prepared with a Zeiss NVision 40 focused ion beam (FIB)-SEM. Transmission electron microscopy (TEM) and high-resolution TEM were carried out on Argonne's Chromatic Aberration-Corrected TEM (ACAT) at an accelerating voltage of 200 kV.

In-situ HEXRD: In-situ high-energy X-ray diffraction (HEXRD) characterization during the charge-discharge process was conducted at the 11-ID-C beamline of the Advanced Photon Source (λ = 0.1173 Å). The tested 2032-type coin cells were modified with 3 mm holes on both the cathode and anode caps. Galvanostatic charge-discharge tests were performed using a MACCOR battery testing system. The electrode samples were prepared by directly tearing pieces from the electrodes and securing them with Kapton tape inside an Ar-filled glove box. A standard reference material CeO2 (SRM 674b) was measured to obtain the instrument parameters for sample data analysis. Rietveld refinements were processed using the sequential refinement function in GSAS-II software package to obtain the lattice parameter changes over cycling.

Scanning diffraction X-ray microscopy (SDXM): Scanning diffraction X-ray microscopy was conducted at the Hard X-ray Nanoprobe beamline (3-ID) at the National Synchrotron Light Source II. During the experiments, X-rays were focused to a ~30 nm spot size to illuminate the sample, with the crystal orientation adjusted to excite Bragg diffraction. A pixel-array detector was positioned to capture the diffracted patterns at each scan point, enabling spatially resolved diffraction measurements. The sample was rocked over a two-degree range around the selected Bragg peak, while a 2D raster scan with a 50 nm step size was performed at each rocking angle. A 5-dimensional dataset with each pixel of the 2D image related to a 3D rocking curve was produced. The final image resolution was determined by the convolution of the beam profile with the pixel size (50 × 50 nm^2). Data analysis was carried out using customized Python scripts.

Full-field transmission X-ray microscopy (TXM) imaging and 3D tomography: Transmission X-ray microscopy imaging was conducted at 18-ID FXI beamline of NSLS-II of Brookhaven National Laboratory and generate 3D nano-XANES datasets. For each energy point across the XANES spectrum, 3D tomographic reconstructions were obtained from a series of projection images captured while rotating the sample from 0° to 180°. These projections were collected at fine angular intervals to ensure accurate reconstruction of the internal structure. The resulting voxel resolution of the tomographic reconstructions was 40 nm, allowing for detailed visualization of nanoscale chemical and structural variations within the sample. Data processing involved phase retrieval and tomographic reconstruction using advanced algorithms to enhance contrast and spatial resolution in the 3D dataset.

Acknowledgments

Work performed at the Center for Nanoscale Materials and Advanced Photon Source (17-BM and 11-ID-C) and both US DOE Office of Science User Facilities was supported by the US DOE, Office of Basic Energy Sciences, under contract no. DE-AC02-06CH11357. Use of the National Synchrotron Light Source II (beamlines 3-ID, 7-BM and 18-ID) is supported by the US DOE Office of Science User Facility operated by Brookhaven National Laboratory under contract no. DE-SC0012704. J.Wang and Y.S.M. acknowledge the startup funding from the Pritzker School of Molecular Engineering in University of Chicago that supported J.Wang's full graduate fellowship.

Author contributions

J.Wang, T.Liu, Y.S.M., and K.A. conceived the idea and designed the experiments. J.Wang and T.Liu synthesized all the materials and conducted electrochemical measurements. L.Y. and J.Wen carried out the SEM and TEM results. T.Liu, J.Wang, M.V.H., W. X. and T.Li performed *ex-situ/in-situ* synchrotron HEXRD and analysis. L.M., J.Wang, W.H. and H.Z. performed *ex-situ* XAS experiment and data analysis. X.H. and L.L. conducted the SDXM and data analysis. X.X., W.H., J.Wang, T. Z., and R.A. performed TXM and data analysis. T.Liu, J.Wang, Y.S.M. and K.A. wrote the manuscript and all authors edited the manuscript.

Competing interests

The authors declare no competing interests.

Data and materials availability

All data is available in the manuscript or the supplementary materials.

Reference

1. Li, M., Lu, J., Chen, Z., Amine, K. 30 Years of lithium-ion batteries. *Adv. Mater.* **30**, 1800561 (2018).
2. Schmuch, R., Wagner, R., Hörpel, G., Placke, T., Winter, M. Performance and cost of materials for lithium-based rechargeable automotive batteries. *Nat. Energy* **3**, 267-278 (2018).
3. Li, W., Erickson, E. M., Manthiram, A. High-nickel layered oxide cathodes for lithium-based automotive batteries. *Nat. Energy* **5**, 26-34 (2020).
4. Goodenough, J. B., Park, K. S. The Li-ion rechargeable battery: a perspective. *J. Am. Chem. Soc.* **135**, 1167-1176 (2013).

5. Liu, T., *et al.* Rational design of mechanically robust Ni-rich cathode materials via concentration gradient strategy. *Nat. Commun.* **12**, 6024 (2021).
6. Yan, P., Zheng, J., Gu, M., Xiao, J., Zhang, J. G., Wang, C. M. Intragranular cracking as a critical barrier for high-voltage usage of layer-structured cathode for lithium-ion batteries. *Nat. Commun.* **8**, 14101 (2017).
7. Bi, Y., *et al.* Reversible planar gliding and microcracking ina single-crystalline Ni-rich cathode. *Science* **370**, 1313-1317 (2020).
8. Zhang, R., *et al.* Compositionally complex doping for zero-strain zero-cobalt layered cathodes. *Nature* **610**, 67-73 (2022).
9. Lin, F., *et al.* Surface reconstruction and chemical evolution of stoichiometric layered cathode materials for lithium-ion batteries. *Nat. Commun.* **5**, 3529 (2014).
10. Lee, S., Su, L., Mesnier, A., Cui, Z., Manthiram, A. Cracking vs. surface reactivity in high-nickel cathodes for lithium-ion batteries. *Joule* **7**, 2430-2444 (2023).
11. Yan, P., *et al.* Tailoring grain boundary structures and chemistry of Ni-rich layered cathodes for enhanced cycle stability of lithium-ion batteries. *Nat. Energy* **3**, 600-605 (2018).
12. Xu, G.‐L., Liu, X., Daali, A., Amine, R., Chen, Z., Amine, K. Challenges and strategies to advance high-energy nickel-rich layered lithium transition metal oxide cathodes for harsh operation. *Adv. Funct. Mater.* **30**, 2004748 (2020).
13. Zhou, Y. N., *et al.* Tuning charge-discharge induced unit cell breathing in layer-structured cathode materials for lithium-ion batteries. *Nat. Commun.* **5**, 5381 (2014).
14. Ryu, H.-H., Park, K.-J., Yoon, C. S., Sun, Y.-K. Capacity Fading of Ni-Rich Li[NixCoyMn1‐x‐y]O2 ($0.6 \leqslant x \leqslant 0.95$) Cathodes for High-Energy-Density Lithium-Ion Batteries: Bulk or Surface Degradation? *Chem. Mater.* **30**, 1155-1163 (2018).
15. Li, W., Asl, H. Y., Xie, Q., Manthiram, A. Collapse of $LiNi_{(1-x-y)}Co_{(x)}Mn_{(y)}O_{(2)}$ lattice at deep charge irrespective of nickel content in lithium-ion batteries. *J. Am. Chem. Soc.* **141**, 5097-5101 (2019).
16. Xu, C., *et al.* Bulk fatigue induced by surface reconstruction in layered Ni-rich cathodes for Li-ion batteries. *Nat. Mater.* **20**, 84-92 (2021).
17. Mukhopadhyay, A., Sheldon, B. W. Deformation and stress in electrode materials for Li-ion batteries. *Prog. Mater. Sci.* **63**, 58-116 (2014).
18. Stallard, J. C., *et al.* Mechanical properties of cathode materials for lithium-ion batteries. *Joule* **6**, 984-1007 (2022).
19. Liu, T., *et al.* Understanding Co roles towards developing Co-free Ni-rich cathodes for rechargeable batteries. *Nat. Energy* **6**, 277-286 (2021).

20. Zhao, X., Ceder, G. Zero-strain cathode materials for Li-ion batteries. *Joule* **6**, 2683-2685 (2022).

21. Xu, G-L.*, et al.* Building ultraconformal protective layers on both secondary and primary particles of layered lithium transition metal oxide cathodes. *Nat. Energy* **4**, 484-494 (2019).

22. Han, Q., Yu, H., Cai, L., Chen, L., Li, C., Jiang, H. Unique insights into the design of low-strain single-crystalline Ni-rich cathodes with superior cycling stability. *PNAS* **121**, e2317282121 (2024).

23. Yu, H.*, et al.* Surface enrichment and diffusion enabling gradient-doping and coating of Ni-rich cathode toward Li-ion batteries. *Nat. Commun.* **12**, 4564 (2021).

24. Goonetilleke, D., Riewald, F., Kondrakov, A. O., Janek, J., Brezesinski, T., Bianchini, M. Alleviating anisotropic volume variation at comparable Li utilization during cycling of Ni-rich, Co-free layered oxide cathode materials. *J. Phys. Chem. C* **126**, 16952-16964 (2022).

25. Li, H., Cormier, M., Zhang, N., Inglis, J., Li, J., Dahn, J. R. Is cobalt needed in Ni-rich positive electrode materials for lithium ion batteries? *J. Electrochem. Soc.* **166**, A429-A439 (2019).

26. Olivetti, E. A., Ceder, G., Gaustad, G. G., Fu, X. Lithium-ion battery supply chain considerations: analysis of potential bottlenecks in critical metals. *Joule* **1**, 229-243 (2017).

27. Aishova, A., Park, G.-T., Yoon, C. S., Sun, Y.-K. Cobalt-free high-capacity Ni-rich layered $Li[Ni_{0.9}Mn_{0.1}]O_2$ cathode. *Adv. Energy Mater.* **10**, 1903179 (2019).

28. Sun, Y. K., Lee, D. J., Lee, Y. J., Chen, Z., Myung, S. T. Cobalt-free nickel rich layered oxide cathodes for lithium-ion batteries. *ACS Appl. Mater. Interfaces* **5**, 11434-11440 (2013).

29. Park, G.-T., Namkoong, B., Kim, S.-B., Liu, J., Yoon, C. S., Sun, Y.-K. Introducing high-valence elements into cobalt-free layered cathodes for practical lithium-ion batteries. *Nat. Energy* **7**, 946-954 (2022).

30. Li, W., Lee, S., Manthiram, A. High-nickel NMA: a cobalt-free alternative to NMC and NCA cathodes for lithium-ion batteries. *Adv. Mater.* **32**, 2002718 (2020).

31. Mu, L.*, et al.* Dopant distribution in Co-free high-energy layered cathode materials. *Chem. Mater.* **31**, 9769-9776 (2019).

32. Qian, G.*, et al.* Single-crystal nickel-rich layered-oxide battery cathode materials: synthesis, electrochemistry, and intra-granular fracture. *Energy Storage Mater.* **27**, 140-149 (2020).

33. Langdon, J., Manthiram, A. A perspective on single-crystal layered oxide cathodes for lithium-ion batteries. *Energy Storage Mater.* **37**, 143-160 (2021).

34. Ge, M.*, et al.* Kinetic limitations in single-crystal high-nickel cathodes. *Angew. Chem. Int. Ed.* **60**, 17350-17355 (2021).

35. Zou, Y. G.*, et al.* Mitigating the kinetic hindrance of single-crystalline Ni-rich cathode via surface gradient penetration of tantalum. *Angew. Chem. Int. Ed.* **60**, 26535-26539 (2021).

36. Huang, W., *et al*. Unrecoverable lattice rotation governs structural degradation of single-crystalline

cathodes. *Science.* **384**, 912-919 (2024).

37. Liu, J.*, et al.* Understanding the synthesis kinetics of single-crystal Co-free Ni-rich cathodes. *Angew Chem Int. Ed.* **62**, e202302547 (2023).

38. Fan, X.*, et al.* In situ inorganic conductive network formation in high-voltage single-crystal Ni-rich cathodes. *Nat. Commun.* **12**, 5320 (2021).

39. Sun, J.*, et al.* The origin of high-voltage stability in single-crystal layered Ni-rich cathode materials. *Angew. Chem. Int. Ed.* **61**, e202207225 (2022).

40. Kim, K.-E.*, et al.* Enhancing high-voltage structural stability of single-crystalline Ni-rich $LiNi_{0.9}Mn_{0.05}Co_{0.05}O_2$ cathode material by ultrathin Li-rich oxide layer for lithium-ion batteries. *J. Power Sources* **601**, 234300 (2024).

41. Zheng, J.*, et al.* Ni/Li disordering in layered transition metal oxide: electrochemical impact, origin, and control. *Acc. Chem. Res.* **52**, 2201-2209 (2019).

42. Radin, M. D.*, et al.* Narrowing the gap between theoretical and practical capacities in Li‐ion layered oxide cathode materials. *Adv. Energy Mater.* **7**, 1602888 (2017).

43. Zheng, S.*, et al.* Correlation between long range and local structural changes in Ni-rich layered materials during charge and discharge process. *J. Power Sources* **412**, 336-343 (2019).

44. Li, J., Downie, L. E., Ma, L., Qiu, W., Dahn, J. R. Study of the failure mechanisms of $LiNi_{0.8}Mn_{0.1}Co_{0.1}O_2$ cathode material for lithium ion batteries. *J. Electrochem. Soc.* **162**, A1401-A1408 (2015).

45. Li, H., Zhang, N., Li, J., Dahn, J. R. Updating the structure and electrochemistry of Li_xNiO_2 for $0 \leqslant x \leqslant 1$. *J. Electrochem. Soc.* **165**, A2985-A2993 (2018).

46. Spence, S. L.*, et al.* Mapping lattice distortions in $LiNi_{0.5}Mn_{1.5}O_4$ cathode materials. *ACS Energy Lett.* **7**, 690-695 (2022).

47. Yu, H.*, et al.* Restraining the escape of lattice oxygen enables superior cyclic performance towards high-voltage Ni-rich cathodes. *Natl. Sci. Rev.* **10**, nwac166 (2023).

48. Sun, H.-H., Manthiram, A. Impact of microcrack generation and surface degradation on a nickel-rich layered $Li[Ni_{0.9}Co_{0.05}Mn_{0.05}]O_2$ cathode for lithium-ion batteries. *Chem. Mater.* **29**, 8486-8493 (2017).

49. House, R. A.*, et al.* What triggers oxygen loss in oxygen redox cathode materials? *Chem. Mater.* **31**, 3293-3300 (2019).

50. Lee, W.*, et al.* Advances in the cathode materials for lithium rechargeable batteries. *Angew. Chem. Int. Ed.* **59**, 2578-2605 (2020).

Figures

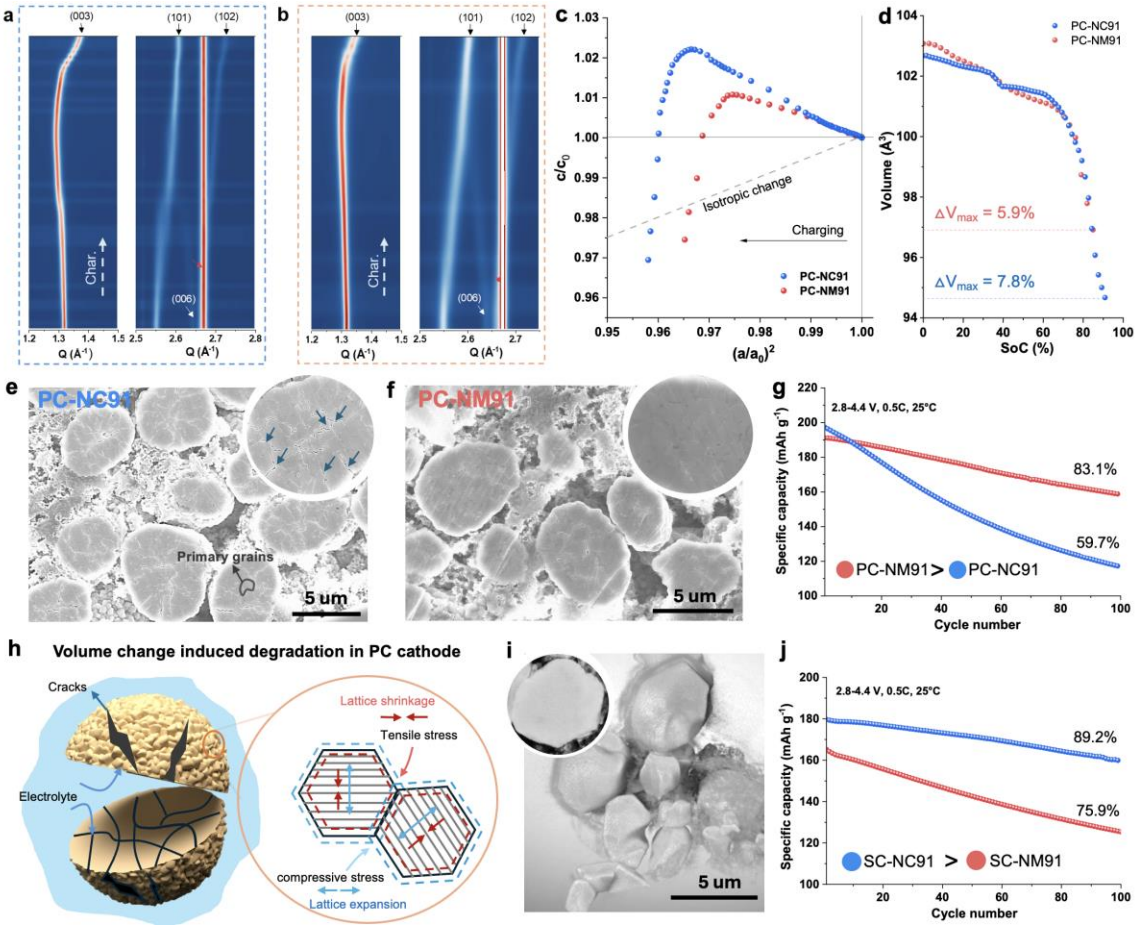

Fig. 1 | Mechanical characterization and electrochemical performance of PC cathodes. **a,b,** 2D contour plots of in situ XRD for the phase evolution of PC-NC91 (**a**) and PC-NM91 (**b**) during the initial cycle at a current rate of C/10. The red arrows indicate the diffraction signals arising from the Al foil current collector. **c.** Plot of c/c_0 versus $(a/a_0)^2$ for both PC-NC91 and PC-NM91. The grey line indicates the isotropic shrinkage of crystal structure. **d.** Plot of lattice volume change during charging for both PC-NC91 and PC-NM91. **e,f,** FIB-SEM images of cycled PC-NC91 (**e**) and cycled PC-NM91 (**f**). **g.** Cycling performance comparison for the two PC cathodes. **h.** Schematic illustration of mechanical degradation mode in PC Ni-rich cathodes. **i,** 3D tomography image for SC-NC91, inserted with the FIB-SEM image showing the grain boundary-free configuration. **j.** Cycling performance comparison for the SC-NC91 and SC-NM91.

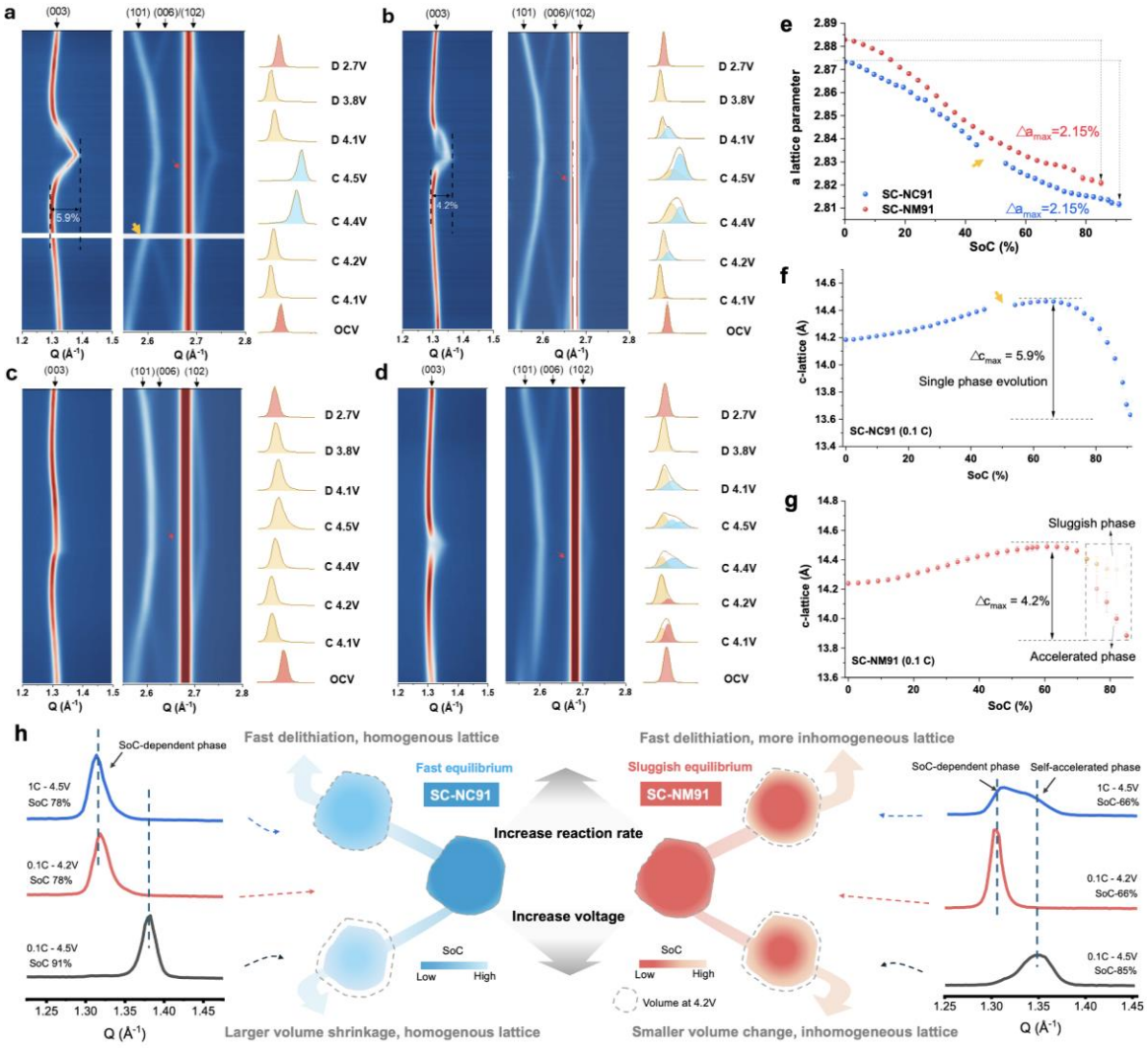

Fig. 2 | Phase evolutions of SC cathodes at different reaction rate. **a,b,** Two-dimensional (2D) contour plots of in situ XRD for the structural evolution of SC-NC91 (**a**) and SC-NM91 (**b**) during the initial cycle using a current rate of C/10. **c,d,** 2D contour plots of in situ XRD for the structural evolution of SC-NC91 (**c**) and SC-NM91 (**d**) during the initial cycle using a current rate of 1C. The deconvoluted (003) reflections are shown in the right of each figure (red, yellow, and blue refer to H1, H2, and H3 phase respectively). Impurities marked by red arrows arise from Li metal anode and Al foil current collector. The yellow arrow shows the data gap due to unexpected beam interruption during battery test. **e-g,** The results from Rietveld refinements for a-lattice parameter changes (**e**), c-lattice parameter change for SC-NC91 (**f**) and SC-NM91 (**g**) during the first charge. **h**, Schematic illustration of different phase evolutions of SC Ni-rich cathodes.

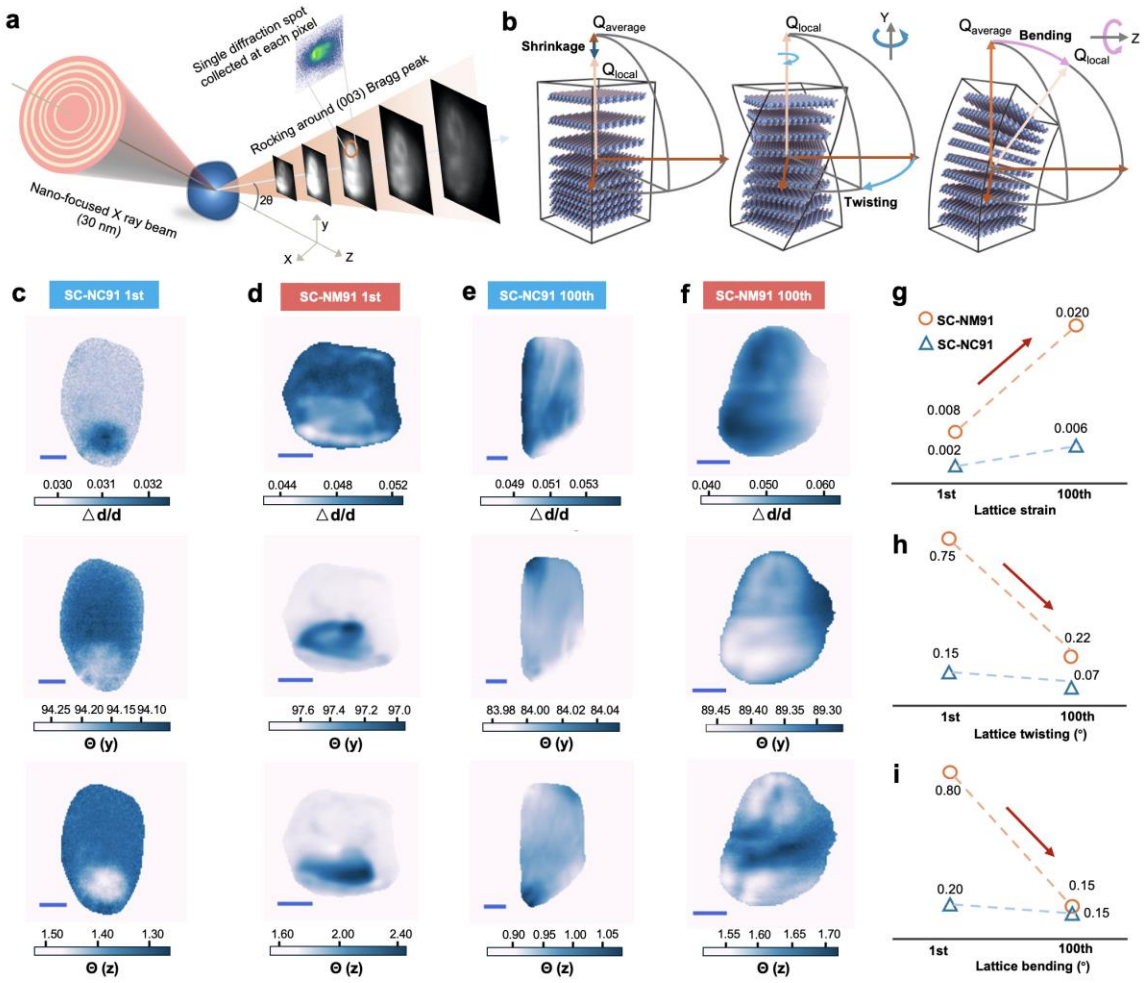

Fig. 3 | Localized lattice distortion profiles inside SC particles at different cycles. a. Schematic of SXDM used in this work. **b.** Schematic illustration of two types of lattice distortions: lattice expansion/contraction (expanding) and lattice rotation (bending and twisting). **c,d.** The difference between local and mean d-spacing mapping, lattice tilt in Y and Z direction for SC-NC91 (**c**) and SC-NM91 (**d**) at a cut off voltage of 4.5V. **e,f**, The difference between local and mean d-spacing mapping, lattice tilt in Y and Z direction for cycled SC-NC91 (**e**) and cycled SC-NM91 (**f**) at the discharged state. **g-i,** Quantitative comparison for lattice strain evolution (**g**), Y twisting (**h**) and Z bending (**i**) of SC-NC91 and SC-NM91 at the 1st and 100th cycles. The scale bar inserted in the figures indicates a length of 1 μm.

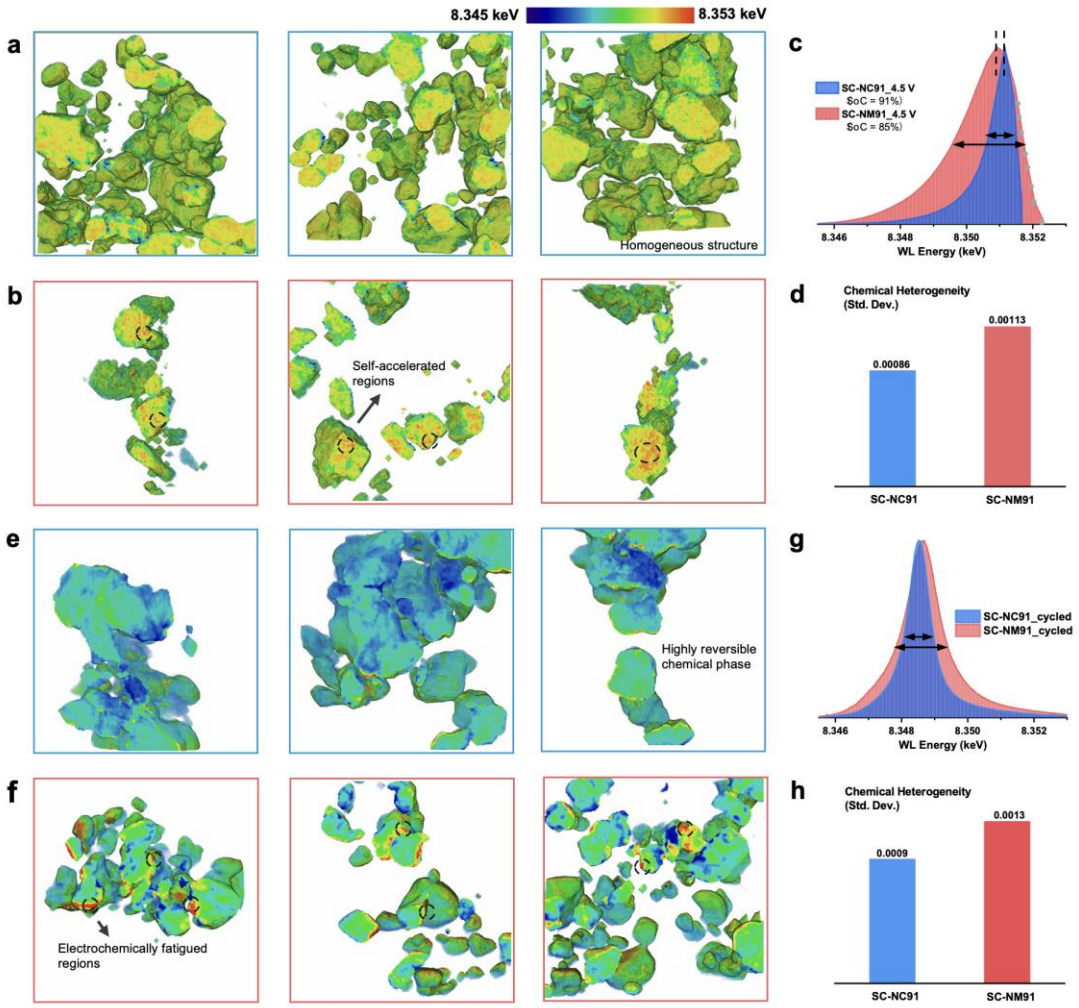

Fig. 4 | 3D chemical phase distribution at charged state and after cycling. **a,b,** The 3D TXM–XANES mappings based on Ni WL peak position for charged SC-NC91 (**a**) and charged SC-NM91 (**b**) at 4.5V. Figures from left to right represent the cross-section views of chemical mapping along xy, yz and xz planes, respectively. **c,** The corresponding WL peak position in statistic based on approximately 10^6 pixels for charged SC-NC91 and SC-NM91. The black arrows indicate the relatively narrow and broad distributions of Ni oxidation states in the two samples. The grey dots show the highly oxidized Ni-related phases existed in charged SC-NM91. The errors for the statistical results are around 0.02 eV. **d,** The chemical heterogeneity shown by calculated standard deviation of the WL peak position in statistic based on (**e**). **e,f,** The 3D TXM–XANES mappings based on WL peak position for cycled SC-NC91 (**e**) and cycled SC-NM91 (**f**). **g,** The corresponding WL peak position in statistic for cycled SC-NC91 and SC-NM91. **h,** The chemical heterogeneity shown by calculated standard deviation of the WL peak position in statistic based on (**g**).

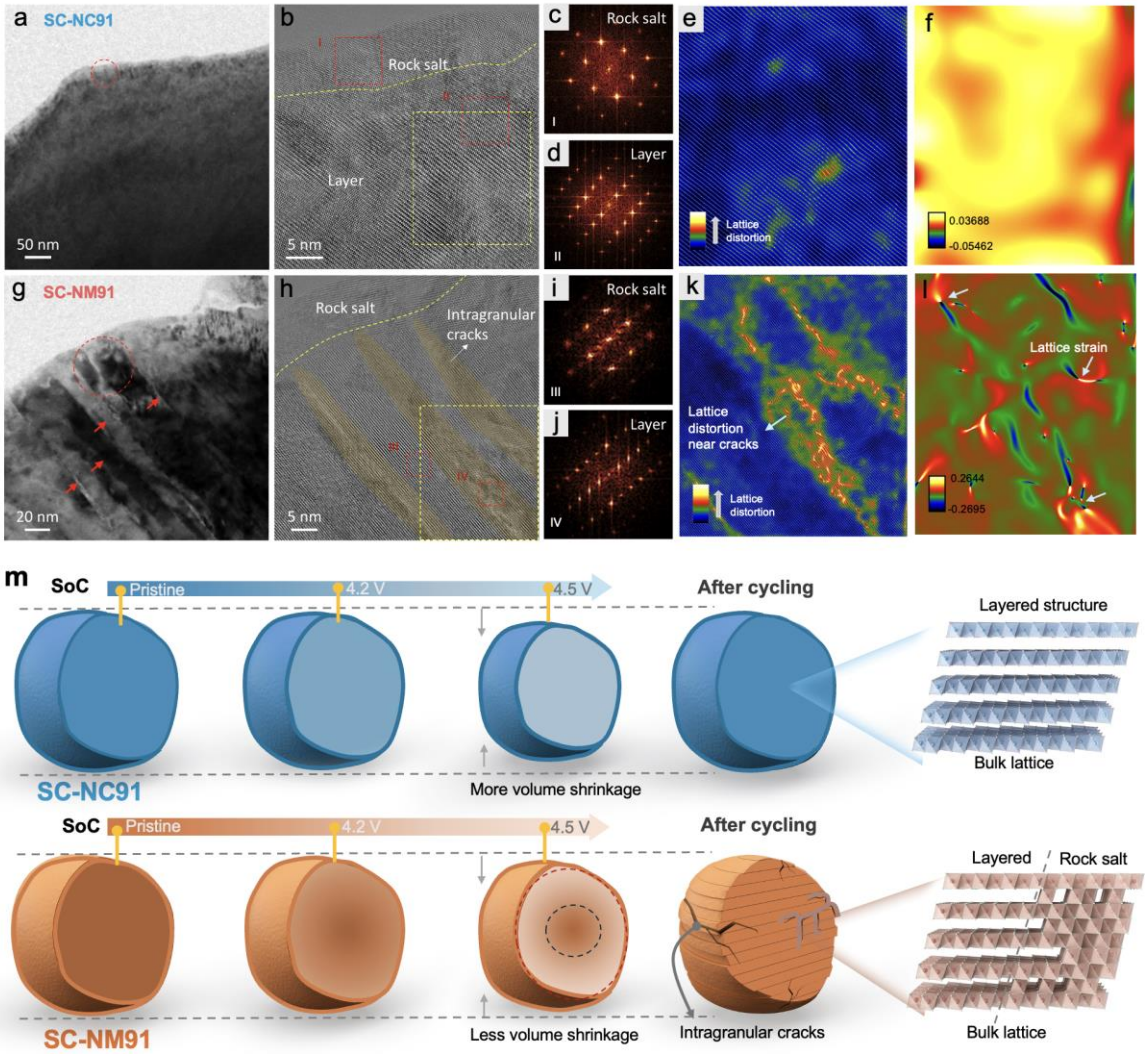

Fig. 5 | Atomic-scale analysis of localized structural and mechanical degradation. **a**,**g,** Low magnification TEM image of SC-NC91 (**a**) and SC-NM91 (**g**) after 100 cycles. **b**,**h,** High magnification TEM image of cycled SC-NC91 (**b**) and cycled SC-NM91(**h**). The selected regions are indicated by red circles in (**a**) and (**g**). **c,d**, Selected area diffraction images are collected from positions indicated by red box in (**b**). **i,j**, Selected area diffraction images from positions indicated by red box in (**h**). **e,k,** Inverse FFT image of cycled SC-NC91 (**e**) and cycled SC-NM91 (**k**) applying mask, as shown in the **Supplementary Fig. 26**. **f,l,** Strain state of SC-NC91 (**f**) and SC-NM91 (**l**) observed by geometric phase analysis (GPA). **m**, The mechanism schematic of chemo-mechanical evolutions for SC-NC91 and SC-NM91. The black circle indicates the kinetically hindered zones. The region between the red and black circles schematically shows the presence of self-accelerating delithiation reaction.